

MODELING SYNTHETIC SPECTRA FOR TRANSITING EXTRASOLAR GIANT PLANETS:
DETECTABILITY OF H₂S AND PH₃ WITH JWST

DONG WANG,¹ YAMILA MIGUEL,² AND JONATHAN LUNINE¹

¹*Department of Astronomy, Space Sciences Building, Cornell University, 14853, Ithaca, NY, USA*

²*Observatoire de la Côte d'Azur Boulevard de l'Observatoire, CS 34229 06304 NICE Cedex 4, France*

Submitted to ApJ

ABSTRACT

JWST's large aperture and wide wavelength coverage will enable it to collect the highest quality transit spectra observed so far. For exoplanetary atmospheres we expect to retrieve the abundance of the most abundant molecules, such as H₂O, CO, and CH₄. Other molecules, such as H₂S and PH₃, have been observed in Jupiter and Saturn but their chemistry and detectability in strongly irradiated planets is highly unknown. In this paper, we make the first effort to study their spectral features in solar composition atmospheres, and evaluate their detectability with JWST. We model the chemistry of phosphorus and sulfur in solar composition atmospheres. Our model includes the effect of vertical transport. Photochemistry effects are not included in our calculations. Using the abundance profiles, we model the JWST transmission and emission spectra for K=6.8 G-type star and for planets with cloud-free solar composition atmospheres. We find PH₃ is detectable at 3 sigma from transmission spectra of the simulated atmosphere with $T_{\text{eq}} < 500\text{K}$ using the NIRCcam LW grism F444W mode with a total observing time of 28.8 hrs. H₂S is detectable at 3 sigma in the transmission and emission spectra for the simulated planet with $T_{\text{eq}} > 1500\text{K}$ using the NIRCcam LW grism F322W2 mode with a total observing time of 24.0 hrs. Our results specifically highlight the importance of including H₂S for future abundances retrieval with JWST. The presence of clouds and hazes challenges the detections of PH₃ and H₂S, but H₂S features are still expected to be present in the emission spectra.

Keywords: planets and satellites, atmospheres — planets and satellites, composition — techniques, spectroscopic

arXiv:1711.00191v1 [astro-ph.EP] 1 Nov 2017

1. INTRODUCTION

The atmospheres of exoplanets can be characterized by transit spectroscopy (e.g., Seager & Sasselov 2000; Hubbard et al. 2001). The transit spectra contain information about the composition and vertical thermal structure of the atmospheres. Interpretation of the transit spectra has led to the discovery of atoms like sodium, potassium (Charbonneau et al. 2002; Redfield et al. 2008; Jensen et al. 2011; Sing et al. 2012, 2015; Nikolov et al. 2014; Wilson et al. 2015), and molecules like H₂O (Deming et al. 2013; Huitson et al. 2013; Mandell et al. 2013; Crouzet et al. 2014; McCullough et al. 2014; Wakeford et al. 2013, 2017; Kreidberg et al. 2014a, 2015; Evans et al. 2016; Line et al. 2016) in the atmospheres of hot Jupiters. Other molecules such as CH₄, CO, CO₂ were also reported in the literature to be detected, however, the detection of these molecules are not confirmed by later observations or other retrieval techniques (e.g., Gibson et al. 2011; Hansen et al. 2014; Line et al. 2014). Currently, the determination of molecular abundances is limited by the quality of the transit spectra (Burrows 2014).

James Webb Space Telescope (JWST)’s large aperture (6.5 m), wide wavelength coverage ($\lambda = 0.6 \sim 28 \mu\text{m}$) and multiple instrument modes will ensure that it will collect the highest quality transit spectra (e.g., Beichman et al. 2014). Greene et al. (2016) simulated how well JWST observations can constrain the temperature-pressure profile and molecular abundances of H₂O, CH₄, CO, CO₂ and NH₃. Other molecules such as H₂S and PH₃ are not included in their calculations. However, H₂S and PH₃ are the primary carriers of sulfur and phosphorus in hydrogen-rich atmospheres (e.g., Visscher et al. 2006), and they potentially contribute to the absorptions in the transit spectra.

PH₃ has been observed in the atmospheres of Jupiter and Saturn (e.g. Fletcher et al. 2009, and references therein). The PH₃ observed in the upper troposphere and stratosphere are supplied by the vertical convection from deeper and hotter regions of the atmosphere where PH₃ is thermochemically stable. The same process may be at work in the exoplanets. H₂S was measured in the troposphere of Jupiter by the Galileo entry probe (Irwin et al. 1998; Wong et al. 2004). H₂S is the primary carrier of sulfur in the atmospheres of Jupiter and Saturn except above a few bars level where H₂S is removed by forming the NH₄SH cloud. For exoplanets with higher stellar irradiation, H₂S may not condense in the upper atmosphere. Therefore, H₂S can potentially contribute to the transit spectra of extrasolar giant planets.

The non-equilibrium chemistry of phosphorus species was not explored in the context of exoplanets with hydrogen-rich atmospheres in the literature. The vertical mixing can drive the chemistry out of equilibrium, just like the case in Jupiter and Saturn. Non-equilibrium chemistry of sulfur in extrasolar giant planets was studied by Zahnle et al. (2009). From their calculations, H₂S is predicted to be the primary carrier of sulfur up to ~ 10 mbar. Above 10 mbar, photochemistry is at work and the abundance of H₂S decreases at higher altitude.

In this paper, we model the non-equilibrium chemistry of phosphorus in the hydrogen-rich atmospheres of exoplanets. We also model the non-equilibrium chemistry of C/N/O/S bearing species in order to get the vertical profiles of major molecules in the atmospheres. To evaluate whether H₂S and PH₃ can be detected by JWST transit observations, we modeled the synthetic transmission and emission spectra with simulated noise levels.

The paper is organized as the follows. In section 2, we describe our chemical model, synthetic spectra model, and JWST noise model. In section 3, we present our results on the computed abundance profiles of major C/N/O/S/P bearing species. In section 4, we present the synthetic transit spectra for four planetary systems with different levels of stellar insolation. In section 5, we add simulated JWST noise into the synthetic spectra, and evaluate the detectability of H₂S and PH₃. In section 6, we discuss the implications for JWST transit observations, and limitations of our model. In section 7, we present the conclusions of this paper.

2. METHODOLOGY

In this section, we describe our methodology for modeling the synthetic JWST transit spectra. We first model the chemistry of C/N/O/S/P and identify major species in the atmospheres that are abundant and thus potentially important for the opacity. Then we model the noiseless primary and secondary transit spectra using the computed abundance profiles. Finally we model the transit spectra with simulated JWST noise, and determine whether certain molecules will be spectroscopically detectable by JWST. We detail our methodologies in what follows.

2.1. Chemical model

We use a one-dimensional diffusion-kinetic model developed in Wang et al. (2015, 2016) to compute the vertical profiles of molecular abundances. The code solves the equation

$$\frac{\partial Y_i}{\partial t} = \frac{1}{\rho} \frac{\partial}{\partial z} (\rho K_{\text{eddy}} \frac{\partial Y_i}{\partial z}) + P_i - L_i, \quad (1)$$

where Y_i is the mass fraction of species i , ρ is the density of the atmosphere, z is the vertical coordinate, K_{eddy} is the vertical eddy diffusion coefficient, P_i is the chemical production rate of species i , and L_i is the chemical loss rate of species i . Two physical processes are modeled by the equation. One is the chemical production or loss of species i , and the other is the vertical transport of species i . The mixing ratio of species in the atmospheres is determined by the dynamic balance between these two physical processes.

We neglect the effect of photochemistry. The effect on the chemical abundances is the photo-dissociation of hydrogen-bearing species (e.g., H₂O, CH₄, NH₃) and the production of photochemical products (e.g., C₂H₆, C₂H₂, HCN) (Moses et al. 2011, 2013; Venot et al. 2012; Kopparapu et al. 2012; Agúndez et al. 2014; Miguel & Kaltenegger 2014). Photochemistry changes the abundances only in the upper atmosphere that is at millibar levels. Therefore, we expect our computed abundance profiles are valid below ~ 10 mbar.

The diffusion-kinetic model requires three kinds of input. First is the temperature-pressure ($T - P$) profile; second is a list of thermodynamic properties and a list of reactions between these species; third is the elemental compositions and the eddy diffusion coefficient. We detail how we choose the inputs below.

- $T - P$ profile: we compute the $T - P$ profile using the model developed in Parmentier & Guillot (2014); Parmentier et al. (2015), which is a non-gray analytical model.
- Thermodynamic properties and reaction rates: the thermodynamic properties are used to compute the equilibrium abundances as well as the backward reaction rates. The thermodynamic properties are compiled from Burcat & Ruscic (2005), McBride et al. (1993), Dean & Bozzelli (2000), and Venot (2012). The kinetic network used for modeling the C/N/O/H chemistry is consisting of 108 species and 1000 reactions, originally from Venot et al. (2012). The H/P/O reaction network consists of 24 species and 175 reactions, originally from Twarowski (1995). A more detailed description of the C/N/O/H and H/P/O reaction networks used in this paper can be found in Wang et al. (2016), and both reaction networks can be downloaded at the KIDA database (<http://kida.obs.u-bordeaux1.fr/networks.html>).
- Elemental abundances: we assume that the elemental composition of the atmosphere is solar. The solar elemental abundances are from Asplund et al. (2009).
- Eddy diffusion coefficient: K_{eddy} is used in the one-dimensional chemical models for parameterizing the vertical transport. There is no observational constraint on the eddy diffusion coefficient on exoplanets. However, its values can be approximated by multiplying the vertical convective velocity derived from 3-D General Circulation Models (GCM) with the pressure scale height (e.g., Moses et al. 2011; Venot et al. 2012; Parmentier et al. 2013). This mixing length theory approximation has an uncertainty on the order of 10 in the estimated eddy diffusion coefficient (Smith 1998). In this paper, we choose to use a constant profile for the K_{eddy} , with values equal to $1 \times 10^9 \text{ cm}^2 \text{ s}^{-1}$ throughout the atmospheres. We explore the dependence on K_{eddy} in section 6.

In each simulation, we provide the elemental abundances, the K_{eddy} , and the $T - P$ profile to set up the code, then we initialize the Y_i of species with chemical equilibrium mass fractions. Y_i are evolved towards a steady state where the time derivative term in equation (1) is zero. In the code, we terminate the simulation once the relative changes of mole fractions in successive Δt is smaller than 1×10^{-3} , where Δt is the overturning timescale, defined as H^2/K_{eddy} , where H is the pressure scale height at 1 bar level. The output is the vertical profiles of Y_i for each species in the model.

2.2. Synthetic spectra model

To simulate the synthetic spectra of transiting exoplanets, we modified the Smithsonian Astrophysical Observatory 1998 (SAO98) radiative transfer code (see Traub & Stier (1976); Traub & Jucks (2002); Kaltenegger & Traub (2009) and references therein for details). The line-by-line radiative transfer code calculates the atmospheric emergent spectra and also transmission of stellar radiation through the atmosphere with disk-averaged quantities at high spectral resolution. The atmosphere is divided in different layers, where the transmission is calculated using Beer's law. Updates include a new database with molecules relevant for giant planets that include H₂O, CH₄, CO, CO₂, NH₃, N₂, HCN, PH₃, H₂S taken from HITRAN (Rothman et al. 2013) and HITEMP (Rothman et al. 2010) database.

The overall high-resolution spectrum is calculated with 0.1 cm^{-1} wavenumber steps. We smear them out to a resolving power of 100 to simulate the resolution that we will obtain with the MIRI instrument. For NIRISS and NIRC_{am}, we assume the observed spectra are binned to a resolution of 100. The smoothing was done using a triangular smoothing kernel.

We neglected the effect of cloud and hazes. Their influence on our results is discussed in the section 6.

2.3. JWST noise model

2.3.1. Greene et al. (2016) noise model

The noise of primary and secondary transit spectra is simulated following the recipes in Greene et al. (2016). Here we provide a compact summary of the noise modeling methodology, along with parameters in the model, summarized in Table 1. The selected JWST observing modes are from Table 4 of Greene et al. (2016). We did not cover the NIRISS SOSS observing mode. The features of H₂S and PH₃ are not as strong as those of H₂O and hence we expect their effects to be masked by H₂O. Therefore, we do not expect this part of the spectrum to be relevant for detection of PH₃ and H₂S. The NIRCAM instrument with LW grism mode covers the wavelength 2.5 ~ 5.0 μm with a native resolution of ~ 1700; the MIRI instrument with slitless mode covers the wavelength 5.0 ~ 11 μm with a resolution of ~ 100. We adopted a cutoff at 11 μm for MIRI slitless mode because the transmission becomes low at longer wavelength (Kendrew et al. 2015). The selected JWST modes provide a wavelength coverage between 2.5 and 11 μm. We choose a binned resolution of R = 100 for all modes to ensure each bin contains enough photons in our simulation.

There are four noise components: the signal photon shot noise, the background photon shot noise, the detector noise, and the systematic noise. The equations for computing each component are from Greene et al. (2016). For completeness, we present these equations below, and describe how we choose the parameter values in these equations.

- The number of signal photons in each spectral bin is computed following the equation

$$S_\lambda = F_\lambda A_{\text{tel}} t \frac{\lambda^2}{hcR} \tau, \quad (2)$$

where S_λ is the number of signal photons in each spectral bin, F_λ is the flux of the signal as received at the telescope, A_{tel} is area of the aperture of JWST, t is the integration time, R is the binned spectral resolution, and τ is the total system transmission. The integration time t is adopted as the full transit duration T_{14} (assuming equal integration time for both in and out transit). The transmission τ is sensitive to wavelength and is obtained from the JWST documentation (<https://jwst-docs.stsci.edu/display/JTI/NIRCam+Filters>). The signal flux F_λ is measured at three configurations, namely, in-transit, out-transit, and in-

eclipse. We assume the in-transit and out-transit integration time is unity. The signal shot noise is equal to the square root of S_λ .

- The background signal is computed following the equation

$$B_\lambda = b_\lambda t A_{\text{pix}} n_{\text{pix}} R_{\text{native}} / R, \quad (3)$$

where B_λ is the background photon numbers in each spectral bin, b_λ is the background electron flux, A_{pix} is the area subtended by each pixel, n_{pix} is two times the number of spacial pixels covered by the spectrum, and R_{native} is the native resolution of the spectrum before binning. The values of above parameters used in this simulation are summarized in Table 1. The background shot noise is equal to the square root of B_λ .

- The total detector noise in single transit observation is calculated as

$$N_{d,\text{tot}} = N_d \sqrt{n_{\text{pix}} n_{\text{ints}} R_{\text{native}} / R}, \quad (4)$$

where N_d is the total detector noise in one integration, and n_{ints} is the number of integrations in one transit observation. The parameter n_{ints} depends on the total transit duration, the brightness limit of each instrument mode, and the brightness of the star. The parameter values are summarized in Table 1.

- The systematic noise cannot be reduced by summing over more observations. We adopted the systematic noise floor as suggested by Greene et al. (2016), as presented in Table 1.

The four noise components are combined quadratically to compute the total noise in each spectral bin for a single transit observation.

2.3.2. PandExo noise model

PandExo (<http://pandexo.science.psu.edu:1111/>) is a tool for computing the error of a spectrum given the stellar SED, the planet spectrum, and the transit duration (Batalha et al. 2017). It is built on top of the STScI's Pandeia exposure time calculator (ETC). PandExo does automatic optimization of groups and integrations. We use this tool to compute the errors on our simulated spectra, and as a validation of our parameters in the Greene et al. (2016) noise model.

3. RESULTS FOR ABUNDANCES PROFILES

In this section, we present our results for the chemistry of C/N/O/S/P species. Temperature and pressure are

the most important factors for determining the molecular abundances. The chemistry is very different for differently irradiated atmospheres. We simulate the atmospheres with different equilibrium temperatures (500 K, 750 K, 1000 K, 1500 K, 2000 K). The T - P profiles used in the calculations are shown in Fig. 1. The vertical eddy diffusion coefficient used is $1 \times 10^9 \text{ cm}^2 \text{ s}^{-1}$, and the composition is assumed to be solar. In the following subsections, we present the computed vertical abundance profiles for $T_{\text{eq}} = 500 \text{ K}$, 1000 K , 1500 K , and 2000 K .

3.1. Results for phosphorus species

Assuming solar elemental abundances for phosphorus, hydrogen, and oxygen, we compute the abundance profiles of H/P/O bearing species for different levels of insolation. We present our results for the phosphorus chemistry in Fig. 2. The most abundant H/P/O bearing species are PH₃, PH₂, PH, HOPO, H₃PO₄, and P₂. For solar composition atmospheres with $T_{\text{eq}} = 500 \text{ K}$ and $T_{\text{eq}} = 1000 \text{ K}$, the abundances are out of chemical equilibrium due to the effect of vertical mixing. For solar composition atmospheres with $T_{\text{eq}} = 1500 \text{ K}$ and $T_{\text{eq}} = 2000 \text{ K}$, the abundances are in chemical equilibrium. The vertical mixing still exists, however, the mixing time scale is longer than the chemical timescale, and the abundances quickly re-equilibrate after mixing. The major phosphorus species are different for different levels of insolation. For a solar composition atmosphere with $T_{\text{eq}} = 500 \text{ K}$, the dominant phosphorus-containing species is PH₃. This is similar to Jupiter, which has an equilibrium temperature at approximately 160 K. For a solar composition atmosphere with $T_{\text{eq}} = 1000 \text{ K}$, PH₃ and P₂ are the most abundant phosphorus containing species above 1 bar. Below 1 bar, PH₃ is still the dominant species. At this temperature, part of the PH₃ is thermally decomposed into PH₂. The reactions between radicals can produce molecules with two or more phosphorus atoms such as P₂. At $T_{\text{eq}} = 1500 \text{ K}$ and 2000 K , the temperature is high enough that most PH₃ is thermally decomposed into PH₂ and PH. The photodissociation of PH₃ is potentially important at low pressure levels. For Jupiter and Saturn, the PH₃ abundance decreases near 0.1 bar level (Fletcher et al. 2009). There is no PH₃ photochemical modeling for hot Jupiters. In our case of solar composition Jupiter-size planets, we assume our abundance profile is valid below 0.1 bar. Above 0.1 bar, the profile is subject to change due to photodissociation.

3.2. Results for sulfur species

Assuming solar composition atmospheres, we compute the equilibrium abundances of sulfur species along the

T - P profile in order to identify the most abundant sulfur bearing species. We consider species H₂S, HS, H₂S₂, CH₃SH, S, S₂, SO, SO₂, CS, CS₂, COS, and SN. The results are shown in Fig. 3. For solar composition atmospheres with $T_{\text{eq}} = 500 \text{ K}$, 1000 K , and 1500 K , H₂S is the dominant species at pressure levels between 1×10^{-4} bar and 1×10^4 bar. For solar composition atmospheres with $T_{\text{eq}} = 2000 \text{ K}$, H₂S is the dominant species below 0.01 bar. Above 0.01 bar, atomic S is the dominant species. Since vertical mixing has the effect of homogenizing the abundances, the addition of vertical mixing into the model is not expected to change the result for H₂S. However, we ignore the effect of photochemistry, which may affect the vertical profile at low pressure levels. Zahnle et al. (2009, 2016) have done photochemical modeling of sulfur species in the atmospheres of hot Jupiters and warm Jupiters. From their calculations, H₂S is largely photo-dissociated at $P \gtrsim 0.01$ bar, but remains the dominant sulfur carrier at $P \lesssim 0.01$ bar. Zahnle et al. (2009) showed that the abundances are not sensitive to temperature and insolation over the parameter ranges ($T = 1200 \sim 2000 \text{ K}$ and $I = 1 \sim 1000$). Following those results, we assume that H₂S is the dominant sulfur bearing species below 0.01 bar in our calculations.

3.3. Results for C/N/O/H species

It is necessary to carefully model the contribution of C/N/O/H bearing species to the transit spectra if we want to identify spectral features of H₂S and PH₃. Molecules such as H₂O or CO are more abundant than H₂S and PH₃, and thus contribute the most to the transit spectra. In order to find molecules that are more abundant than H₂S and PH₃, we performed independent calculations for C/N/O/H chemistry. Our results are in general consistency with results reported in the literature (e.g., Moses et al. 2011; Venot et al. 2012; Miguel & Kaltenecker 2014; Hu & Seager 2014). We find the major C/N/O/H bearing molecules are H₂O, CO, CH₄, CO₂, N₂, NH₃, and HCN. These molecules must be included in the spectra calculation in order to cover all important opacity sources. We present our computed vertical profile of these molecules along with PH₃ and H₂S in Fig. 4. The results are shown for four different levels of stellar insolation.

For solar composition atmospheres with $T_{\text{eq}} = 500 \text{ K}$, the most abundant species are H₂O, CH₄, NH₃, H₂S, N₂ and PH₃. The abundances are nearly homogeneous in the vertical direction down to ~ 10 bars. The atmosphere is strongly homogenized by vertical mixing, and species are in a disequilibrium state. CH₄ is the primary carbon-bearing species, H₂O is the primary oxygen-

bearing species, NH_3 is the primary nitrogen-bearing species, H_2S is the primary sulfur-bearing species, and PH_3 is the primary phosphorus-bearing species.

For solar composition atmospheres with $T_{\text{eq}} = 1000$ K, the most abundant species are H_2O , CO , CH_4 , N_2 , NH_3 , H_2S , HCN , and PH_3 . Abundances are nearly homogeneous down to 1-10 bars due to the effect of vertical mixing. CO carries about 2/3 of the total carbon abundance, and CH_4 carries the other 1/3 of the total carbon abundance. H_2O is the dominant oxygen bearing species. N_2 and NH_3 each carries about 1/2 of the total nitrogen abundance. This temperature marks the transition temperature for CO/CH_4 conversion and N_2/NH_3 conversion. For $T_{\text{eq}} \lesssim 1000$ K, CH_4 and NH_3 are the major carbon and nitrogen carriers; for $T_{\text{eq}} \gtrsim 1000$ K, CO and N_2 are the major carbon and nitrogen carriers.

For solar composition atmospheres with $T_{\text{eq}} = 1500$ K, the most abundant species are CO , H_2O , N_2 , and H_2S . CO is the primary carrier of both oxygen and carbon. The rest of the oxygen is in the form of H_2O . N_2 is the primary carrier of nitrogen. CH_4 and NH_3 are much less abundant in the atmospheres.

For solar composition atmospheres with $T_{\text{eq}} = 2000$ K, the most abundant species are CO , H_2O , N_2 , and H_2S . The abundances are nearly in chemical equilibrium due to the high temperature. CH_4 , NH_3 , and PH_3 are much less abundant.

3.4. Influence of insolation

There are three regimes for the abundance profiles depending on the level of insolation. For highly irradiated atmospheres (e.g., $T_{\text{eq}} > 1500$ K), the chemical abundances are in local chemical equilibrium. Therefore, when doing retrieval on atmosphere composition and T - P profile, assumptions of chemical equilibrium should be valid. For moderately irradiated atmospheres (e.g., $T_{\text{eq}} < 1000$ K), the vertical mixing tends to produce a homogeneous abundances in the atmospheres. It should be valid to assume a constant mixing ratio profile when doing atmospheric retrieval. In between is the transition regime when both chemical conversions and vertical mixing are important in the atmospheres. In this regime, the abundance profiles will depend on the vertical eddy diffusion coefficient as well as the T - P profile. In Fig 5, we show the computed abundances at 1 bar level as a function of T_{eq} . From the figure, CO , CO_2 , and N_2 abundances increase as T_{eq} increases, while CH_4 , NH_3 , and PH_3 abundances decrease as T_{eq} increases. H_2O and H_2S abundances remain approximately unchanged relative to the change of T_{eq} . The HCN abundance increases and decreases as T_{eq} increases.

4. RESULTS FOR NOISELESS SPECTRA MODELING

In this section, we present the synthetic primary and secondary transit spectra for three fiducial planets ($T_{\text{eq}} = 500$ K, 1000 K, and 1500 K). The parameters for the planets are summarized in Table 2. The planets are solar composition Jupiter-size planets with different levels of insolation. The vertical T - P profiles for the planets are presented in Fig. 1 and the vertical abundance profiles are presented in Fig 4. The molecules included are H_2O , CO , CH_4 , CO_2 , N_2 , NH_3 , HCN , H_2S and PH_3 .

The spectral features for H_2O , CO , CH_4 , CO_2 , and NH_3 have been explored in the literature (e.g. Greene et al. 2016). From our calculations in section 3, we found that H_2S is the primary carrier of sulfur for all different equilibrium temperatures; PH_3 is the primary carrier of phosphorus for $T_{\text{eq}} < 1000$ K; HCN has a mixing ratio of 1 ppm for solar composition atmospheres with $T_{\text{eq}} = 1000$ K. These molecules are potentially identifiable from the transit spectra. Although HCN is not the primary carrier of either carbon or nitrogen, it is a disequilibrium species and its abundances are indicative of the strength of vertical mixing. Therefore, we also investigate the spectral feature of HCN and see if JWST can potentially detect HCN .

Here we focus on identifying spectral features for PH_3 , H_2S , and HCN in the primary and secondary transit spectra of solar composition Jupiter-size planets. We compare the spectra including all nine species with the spectra with one specific species excluded, in order to find the spectral feature of that specific species.

4.1. PH_3

Fig. 6, we present the primary and secondary transit spectra for the planetary systems in Table 2, with $T_{\text{eq}} = 500$ K, 1000 K, and 1500 K. The planets are assumed to have solar composition atmospheres. The vertical abundance profiles are taken from Fig. 4. We compare the spectra simulated with *all species*, and the spectra simulated with *all species except* PH_3 . The difference between these two spectra indicates the absorption from PH_3 . For an solar composition atmosphere with $T_{\text{eq}} = 500$ K, the absorption from PH_3 occurs between 4 and 5 μm . The absorption depth is about 40 ppm in the primary transit spectra. The absorption is about 20 ppm in the secondary transit spectra. For the atmosphere with $T_{\text{eq}} = 1000\text{K}$, the absorption is about 5 ppm in the primary transit spectra, while in the secondary transit spectra, the absorption is too small to be seen in the figure. For the atmosphere with $T_{\text{eq}} = 1500\text{K}$, there is no apparent PH_3 absorption feature in the spectra.

The lack of PH₃ spectral feature for the solar composition atmospheres with $T_{\text{eq}} = 1000$ K and 1500 K is due to the thermal decomposition of PH₃ under high temperatures. From Fig. 2, for the atmospheres with $T_{\text{eq}} = 500$ K, almost all of the phosphorus are in the form of PH₃; while for the atmospheres with $T_{\text{eq}} = 1000$ K and 1500 K, most phosphorus are in the form of P₂ and PH₂. Therefore, the spectral features of PH₃ are only expected in moderately irradiated atmospheres.

4.2. H₂S

In Fig. 7, we present the synthetic primary and secondary transit spectra for the solar composition atmospheres with $T_{\text{eq}} = 500$ K, 1000 K, and 1500 K in Table 2. We compare the spectra simulated with *all species* and the spectra simulated with *all species except H₂S*. For the atmospheres with $T_{\text{eq}} = 500$ K, the absorption depth is very small. In the primary transit spectra, there is a 5 ppm absorption at $2.6 \sim 2.8 \mu\text{m}$ and a 10 ppm absorption at $3.9 \sim 4.3 \mu\text{m}$. In the secondary transit spectra, there is a 10 ppm absorption at $3.9 \sim 4.3 \mu\text{m}$. For the atmospheres with $T_{\text{eq}} = 1000$ K, the absorption depths are also very small, for both primary transit and secondary transit spectra. For the atmospheres with $T_{\text{eq}} = 1500$ K, the absorption depths are much bigger. In the primary transit spectra, the absorption depth is about 15 ppm at $2.6 \sim 2.8 \mu\text{m}$, and 100 ppm at $3.5 \sim 4.1 \mu\text{m}$. In the secondary spectra, the absorption depth is about 10 ppm at $2.6 \sim 2.8 \mu\text{m}$ and 100 ppm at $3.5 \sim 4.1 \mu\text{m}$.

The spectral feature of H₂S is more prominent in highly irradiated atmospheres. What determines the relevance of H₂S in the spectra is other species. In cold atmospheres, H₂S has to compete with the more abundant NH₃ and CH₄ to absorb photons while in the hottest case those two molecules are less abundant, leaving more space to H₂S to absorb photons and be seen in the spectra. Another factor that may also contribute is the larger pressure scale height in hotter atmospheres.

4.3. HCN

In Fig. 8, we present the synthetic primary and secondary transit spectra for solar composition atmospheres with $T_{\text{eq}} = 500$ K, 1000 K, and 1500 K listed in Table 2. For the atmospheres with $T_{\text{eq}} = 500$ K and 1500 K, there are little absorption from HCN, mainly because the mixing ratio of HCN is very low, as shown in Fig. 4. For the atmospheres with $T_{\text{eq}} = 1000$ K, there are small absorption features between 12 and 16 μm . The absorption depth in the primary transit spectra is about 15 ppm, and the absorption depth in the secondary transit spectra is about 80 ppm.

5. RESULTS FOR JWST TRANSIT SPECTRA MODELING

In this section, we model the JWST spectra for primary and secondary transit observations. The instruments and modes for transit observations are shown in Table 1. The wavelength range modeled is between 2.5 μm and 11 μm . In section 4, we identified spectral features for PH₃, H₂S, and HCN. The spectral feature of PH₃ is between 4 μm and 5 μm , the spectral feature of H₂S is between 3 μm and 4 μm , and the spectral feature of HCN is between 12 μm and 16 μm . The feature of HCN is beyond the limit of MIRI LRS mode (Beichman et al. 2014). In this paper, we focus on the spectra features of H₂S and PH₃.

5.1. Results for JWST noise modeling

We used both PandExo and the Greene et al. (2016) noise model to compute the error on the spectrum. In Fig. 9, we show the noise level as a function of wavelength for a range of instrument modes covering wavelength ranging from 2.5 μm to 11 μm . The parameters of the planetary system being modeled are listed in Table 2. We assume two transits, each with equal in-transit and out-transit integration time. The transit duration is 7.2 hrs, and the total (transit + baseline) time is 14.4 hrs. The number of groups and number of integrations are optimized by the PandExo. Besides the results calculated using PandExo, we also compute the error using the Greene et al. (2016) noise model for the NIRCcam F322W2 mode and F444W mode. The Greene et al. (2016) model gives slightly lower noise levels, but similar to the results by PandExo.

5.2. PH₃

In Fig. 10, we show the synthetic primary and secondary transit spectra with simulated JWST noise and compare the spectra with and without PH₃. The planetary system being modeled is listed in Table 2 with $T_{\text{eq}} = 500$ K. The observation parameters are summarized in Table 3. The spectral absorption feature of PH₃ is between 4.0 and 4.7 μm . In the primary transit spectra, the absorption depth for PH₃ is approximately one standard deviation of the noise. Since there are ~ 10 measurements within this feature, the significance level for detecting PH₃ is more than three sigma. In order to cover the 4.0 – 4.7 μm wavelength range, the NIRCcam LW grism mode with F444W filter can be used in the observation. To achieve this level of error, two transits are needed. The integration time for each transit is about 7.2 hrs. We assume equal integration time for in transit and out of transit, and that leads to a total observing time of 7.2 hrs \times 2 in and out of transit integration \times

2 transits = 28.8 hrs. The absorption feature in the secondary transit spectra is harder to detect since the absorption depth from PH_3 is only about half the standard deviation of the noise. Therefore, it is the most effective for detecting PH_3 to use the primary transit spectra with the NIRCcam LW grism mode and F444W filter, and get the spectra between $3.9 \mu\text{m}$ and $5.0 \mu\text{m}$. However, the feature is very weak and requires long integration time (7.2 hrs) to achieve the error level shown in Fig. 10. Since CH_4 absorption is strong between 4 and $5 \mu\text{m}$, additional observation using the NIRCcam LR F444W may be needed to break the degeneracy between the PH_3 absorption and CH_4 absorption. For higher equilibrium temperatures ($T_{\text{eq}} > 1000 \text{ K}$), the spectral feature of PH_3 is below 5 ppm that JWST is unlikely to detect it.

5.3. H_2S

In Fig. 11, we show the synthetic primary and secondary transit spectra with simulated JWST noise and compare the spectra with and without H_2S . The spectral absorption feature of H_2S is between 3.5 and $4 \mu\text{m}$. We show the spectra with simulated noise for the planetary system in Table 2 with $T_{\text{eq}} = 1500 \text{ K}$. The star in the system is a Sun-like star with K band magnitude of 6.8. The observational parameters are summarized in Table 4. In the primary transit spectra, the absorption depth is about two times the standard deviation of the noise. The shape of the absorption feature can be resolved with the binned spectral resolution of $R \sim 100$. To cover the spectral feature of H_2S , one can use the NIRCcam LW grism mode with F322W2 filter, getting the spectra between $2.4 \mu\text{m}$ and $4.0 \mu\text{m}$. In the secondary transit spectra, the absorption depth is approximately two times the standard deviation of the noise. Therefore, it is also likely to detect H_2S in the secondary transit spectra. The same mode of NIRCcam can be used to obtain the secondary transit spectra. To achieve this level of error, five transits are needed. The integration time for each transit is about 2.4 hrs. We calculate the total observing time in the same way as in section 5.2, to obtain 24.0 hours. Since H_2O absorption is also important in the $2.4 \mu\text{m}$ to $4.0 \mu\text{m}$ region, NIRISS SOSS mode observations may be needed to determine the base and peak of water features, in order to verify the spectra features of H_2S . We only show the case for $T_{\text{eq}} = 1500 \text{ K}$ in Fig. 11, while for atmospheres with lower equilibrium temperature (500 K, 750 K, 1000 K), the absorption from H_2S is below 10 ppm and JWST is unlikely to detect it.

6. DISCUSSION

In this paper, we investigate the phosphorus and sulfur chemistry in solar composition atmospheres of Jupiter-size planets with the effect of vertical mixing, but no photochemistry. We find PH_3 is the primary carrier of phosphorus in solar composition atmospheres with $T_{\text{eq}} \sim 500 \text{ K}$. For solar composition atmospheres with $1000 \text{ K} \lesssim T_{\text{eq}} \lesssim 1500 \text{ K}$, the primary carrier of phosphorus is P_2 . For very highly irradiated solar composition atmospheres ($T_{\text{eq}} \sim 2000 \text{ K}$), phosphorus is mainly sequestered in PH_2 and PH . For sulfur chemistry, we find H_2S is the primary carrier of sulfur for solar composition atmospheres with $T_{\text{eq}} < 2000 \text{ K}$. We also investigate the chemistry of C/N/O/S bearing species for solar composition atmospheres. The most abundant carbon and nitrogen bearing species depend on the level of insolation. For the atmosphere with $T_{\text{eq}} < 1000 \text{ K}$, H_2O , CH_4 and NH_3 are the most abundant molecules; while for the atmosphere with $T_{\text{eq}} > 1000 \text{ K}$, H_2O , CO , and N_2 are the most abundant molecules. With the computed abundance profiles for H_2O , CO , CO_2 , CH_4 , NH_3 , N_2 , H_2S , PH_3 , and HCN , we model the synthetic primary and secondary transit spectra and identify spectral features for PH_3 , H_2S , and HCN . The detectability of PH_3 and H_2S with JWST transit observations are evaluated by simulating the noise levels. We find PH_3 can be detected in the primary transit spectra of solar composition atmospheres with $T_{\text{eq}} \lesssim 500 \text{ K}$ using JWST NIRCcam LW F444W mode, and the total observing time needs to be ~ 28.8 hrs. H_2S can be detected in both primary and secondary spectra of solar composition Jupiter-size planets with $T_{\text{eq}} \gtrsim 1500 \text{ K}$ using JWST NIRCcam LW F322W2 mode with a total observing time of 24.0 hrs.

Our results imply that H_2S is an important absorber in the $3 - 4 \mu\text{m}$ region for solar composition atmospheres with $T_{\text{eq}} > 1500 \text{ K}$. Failure to include H_2S in the retrieval analysis of JWST spectra may lead to the non-fitting of the spectra, or more detrimentally, lead to wrong abundances of other molecules. The effect can only be determined by a full retrieval analysis, which is beyond the scope of this paper. However, we highlight the importance of H_2S in the $3 - 4 \mu\text{m}$ region of transit spectra. PH_3 show little features on the transit spectra of hot Jupiter's atmospheres ($T_{\text{eq}} > 1000 \text{ K}$), but show absorption features between 4 and $5 \mu\text{m}$ in moderately irradiated atmospheres ($T_{\text{eq}} \sim 500 \text{ K}$). Retrieval of molecular abundances for moderately irradiated planets needs to consider the absorption from PH_3 .

We also considered HCN in our model since we find HCN is non-negligible for planets with $T_{\text{eq}} = 1000 \text{ K}$, with a mixing ratio of 1 ppm. Since photochemistry also produces HCN , we expect more HCN in the upper atmospheres. The absorption features of HCN are

mainly between 12 and 16 μm . This wavelength range is beyond the coverage of the MIRI LRS slitless mode. Therefore, we did not discuss further the detectability of HCN with JWST.

Our modeling of JWST transit spectra makes several simplifications, and we discuss the influences below.

- The transit spectra of PH₃ and H₂S are complicated by the presence of clouds or hazes in the atmospheres of extrasolar giant planets. Current observations indicate that clouds or hazes are ubiquitous in the atmospheres of exoplanets (e.g. Pont et al. 2008; Deming et al. 2013; Kreidberg et al. 2014b). Clouds and hazes reduce the amplitude of transmission spectra and thus decrease the molecular spectral features with a negative effect on the determination of molecular abundances. The emission spectra are less affected by the clouds and hazes (e.g., Line et al. 2016). The spectral absorption depth of H₂S in the emission spectra is much greater than the expected noise level. Therefore, the H₂S feature can be detected using the emission spectra for atmospheres with clouds and haze. However, the absorption depth of PH₃ in the emission spectra is smaller than the expected noise level, therefore, the detection of PH₃ will be difficult if the atmosphere is covered by clouds or hazes.
- We neglect the effect of photochemistry on the primary and secondary transit spectra. Photochemistry affects the spectra in two ways. First, photochemistry changes the abundance profiles in the upper atmospheres. The effect on the secondary transit spectra is expected to be small since the absorption in the planetary emission spectra occurs near the 1 bar level. There may be some effects on the primary transit spectra since the light travels a longer path in the transmission spectra than in the emission spectra. Most absorption should still be from more abundant molecules (e.g. H₂O, CH₄, CO, NH₃, H₂S, PH₃) in the atmospheres. The photochemical products (C₂H₆, C₂H₂, HCN) may contribute a small amount of absorption and it is unclear whether JWST is able to detect these photochemical species. The second effect of photochemistry is the production of hazes. The flat transmission spectra for hot Jupiters and super-Earth may be caused by the photochemical hazes in the upper atmospheres. The effect of hazes on the spectra is the shrinking of the spectral amplitude, making the detection of molecules more difficult.

- We assumed a single value of eddy diffusion coefficient in all our simulations. The strength of vertical mixing is highly uncertain on exoplanets. In Fig. 12, we compare the abundances calculated using $K_{\text{eddy}} = 1 \times 10^9 \text{ cm}^2 \text{ s}^{-1}$ and $1 \times 10^8 \text{ cm}^2 \text{ s}^{-1}$. Molecular species such as H₂O and CH₄ are largely unaffected by the strength of vertical mixing since they are the dominant species throughout the atmosphere. For disequilibrium species such as CO and CO₂, the effect is to shift the abundances in the same direction. CO is increased by less than one order of magnitude due to the change of K_{eddy} .
- In this paper, we restrict our study to solar composition atmospheres. However, the elemental composition of exoplanetary atmospheres can be diverse. Jupiter’s atmosphere is enriched in heavy elements relative to solar. It is reasonable to assume extrasolar giant planets have similar enrichment. If all the heavy elements (C,N,O,S,P) are enriched similarly, the shape of the abundance profiles is preserved with only an upward shift. We expect the transmission spectra to have smaller spectral amplitudes since the pressure scale height is expected to be smaller for higher molecular mass atmospheres. This has an adverse effect on detecting molecules. However, higher mean molecular weight often correlates with smaller mass. For Neptune-size planets, the smaller gravity means higher scale height, and larger spectral amplitudes. The opposite effect of gravity and molecular mass on the spectra should rely on detailed modeling of Neptune -size exoplanets, which will be discussed in our next paper. If carbon and oxygen are not similarly enriched, for example C/O different than solar, the composition will be dramatically different for hot atmospheres.

7. CONCLUSIONS

In this paper, we modeled phosphorus and sulfur chemistry in the solar composition atmospheres of Jupiter-size planets with different levels of insolation. We find PH₃ is the primary carrier of phosphorus for atmospheres with $T_{\text{eq}} < 1000 \text{ K}$; P₂ is the primary carrier of phosphorus for T_{eq} greater than 1000 K and smaller than 1500 K; PH and PH₂ are the primary phosphorus bearing species for $T_{\text{eq}} > 2000 \text{ K}$. H₂S is the primary carrier of sulfur for $T_{\text{eq}} < 2000 \text{ K}$. We also compute the abundance profiles of major H/C/N/O/S bearing species. With the computed vertical profiles for H₂O, CO, CO₂, CH₄, NH₃, N₂, HCN, H₂S, and PH₃, we compute the synthetic primary and secondary transit spectra. We focus on identifying the spectral features

for H₂S, PH₃, and HCN. We find spectral features of PH₃ at 4.0 ~ 4.8 μm, H₂S at 2.5 ~ 2.8 μm and 3.5 ~ 4.1 μm, HCN at 12 ~ 16 μm. We then simulated the noise for transits with K = 6.8 G star, and evaluated the detectability of PH₃ and H₂S with JWST observations. We find PH₃ can be detected for solar composition atmospheres with $T_{\text{eq}} \sim 500$ K using the NIRCcam LW F444W mode with a total observing time of 28.8 hrs. We find H₂S can be detected for solar composition atmospheres with $T_{\text{eq}} > 1500$ K using the NIRCcam LW grism F322W2 mode with a total observing time of 24.0 hrs. The detection of PH₃ and H₂S is complicated by

the presence of clouds and hazes. In this case, H₂S may still be detected in the emission spectra, but PH₃ is difficult to detect due to the diminished spectra features by clouds and hazes.

D.W. and J.I.L. acknowledge support from the Juno and JWST projects. Y.M. greatly appreciates the CNES post-doctoral fellowship program.

Software: SAO98 (Traub & Stier 1976; Traub & Jucks 2002; Kaltenecker & Traub 2009), PandExo (Batalha et al. 2017)

REFERENCES

- Agúndez, M., Parmentier, V., Venot, O., Hersant, F., & Selsis, F. 2014, *A&A*, 564, A73
- Asplund, M., Grevesse, N., Sauval, A. J., & Scott, P. 2009, *ARA&A*, 47, 481
- Batalha, N. E., Mandell, A., Pontoppidan, K., et al. 2017, *PASP*, 129, 064501
- Beichman, C., Benneke, B., Knutson, H., et al. 2014, *PASP*, 126, 1134
- Burcat, A., & Ruscic, B. 2005, Third millenium ideal gas and condensed phase thermochemical database for combustion with updates from active thermochemical tables (Argonne National Laboratory Argonne, IL)
- Burrows, A. S. 2014, *Proceedings of the National Academy of Science*, 111, 12601
- Charbonneau, D., Brown, T. M., Noyes, R. W., & Gilliland, R. L. 2002, *ApJ*, 568, 377
- Crouzet, N., McCullough, P. R., Deming, D., & Madhusudhan, N. 2014, *ApJ*, 795, 166
- Dean, A. M., & Bozzelli, J. W. 2000, *Gas-Phase Combustion Chemistry* (New York, NY: Springer New York), 125–341.
http://dx.doi.org/10.1007/978-1-4612-1310-9_2
- Deming, D., Wilkins, A., McCullough, P., et al. 2013, *ApJ*, 774, 95
- Evans, T. M., Sing, D. K., Wakeford, H. R., et al. 2016, *ApJL*, 822, L4
- Fletcher, L. N., Orton, G. S., Teanby, N. A., & Irwin, P. G. J. 2009, *Icarus*, 202, 543
- Gibson, N. P., Pont, F., & Aigrain, S. 2011, *MNRAS*, 411, 2199
- Greene, T. P., Line, M. R., Montero, C., et al. 2016, *ApJ*, 817, 17
- Hansen, C. J., Schwartz, J. C., & Cowan, N. B. 2014, *MNRAS*, 444, 3632
- Hu, R., & Seager, S. 2014, *The Astrophysical Journal*, 784, 63
- Hubbard, W. B., Fortney, J. J., Lunine, J. I., et al. 2001, *ApJ*, 560, 413
- Huitson, C. M., Sing, D. K., Pont, F., et al. 2013, *MNRAS*, 434, 3252
- Irwin, P. G. J., Weir, A. L., Smith, S. E., et al. 1998, *J. Geophys. Res.*, 103, 23001
- Jensen, A. G., Redfield, S., Endl, M., et al. 2011, *ApJ*, 743, 203
- Kaltenecker, L., & Traub, W. A. 2009, *The Astrophysical Journal*, 698, 519
- Kendrew, S., Scheithauer, S., Bouchet, P., et al. 2015, *PASP*, 127, 623
- Kopparapu, R. k., Kasting, J. F., & Zahnle, K. J. 2012, *ApJ*, 745, 77
- Kreidberg, L., Bean, J. L., Désert, J.-M., et al. 2014a, *ApJL*, 793, L27
- . 2014b, *Nature*, 505, 69
- Kreidberg, L., Line, M. R., Bean, J. L., et al. 2015, *ApJ*, 814, 66
- Line, M. R., Knutson, H., Wolf, A. S., & Yung, Y. L. 2014, *ApJ*, 783, 70
- Line, M. R., Stevenson, K. B., Bean, J., et al. 2016, *AJ*, 152, 203
- Mandell, A. M., Haynes, K., Sinukoff, E., et al. 2013, *ApJ*, 779, 128
- McBride, B. J., Gordon, S., & Reno, M. A. 1993, *Coefficients for calculating thermodynamic and transport properties of individual species*, Tech. rep.
- McCullough, P. R., Crouzet, N., Deming, D., & Madhusudhan, N. 2014, *ApJ*, 791, 55
- Miguel, Y., & Kaltenecker, L. 2014, *ApJ*, 780, 166
- Moses, J. I., Madhusudhan, N., Visscher, C., & Freedman, R. S. 2013, *ApJ*, 763, 25
- Moses, J. I., Visscher, C., Fortney, J. J., et al. 2011, *ApJ*, 737, 15

- Nikolov, N., Sing, D. K., Pont, F., et al. 2014, *MNRAS*, 437, 46
- Parmentier, V., & Guillot, T. 2014, *A&A*, 562, A133
- Parmentier, V., Guillot, T., Fortney, J. J., & Marley, M. S. 2015, *A&A*, 574, A35
- Parmentier, V., Showman, A. P., & Lian, Y. 2013, *A&A*, 558, A91
- Pont, F., Knutson, H., Gilliland, R. L., Moutou, C., & Charbonneau, D. 2008, *MNRAS*, 385, 109
- Redfield, S., Endl, M., Cochran, W. D., & Koesterke, L. 2008, *ApJL*, 673, L87
- Rothman, L., Gordon, I., Barber, R., et al. 2010, *Journal of Quantitative Spectroscopy and Radiative Transfer*, 111, 2139
- Rothman, L. S., Gordon, I. E., Babikov, Y., et al. 2013, *Journal of Quantitative Spectroscopy and Radiative Transfer*, 130, 4
- Seager, S., & Sasselov, D. D. 2000, *ApJ*, 537, 916
- Sing, D. K., Huitson, C. M., Lopez-Morales, M., et al. 2012, *MNRAS*, 426, 1663
- Sing, D. K., Wakeford, H. R., Showman, A. P., et al. 2015, *MNRAS*, 446, 2428
- Smith, M. D. 1998, *Icarus*, 132, 176
- Traub, W., & Jucks, K. 2002, M. Mendillo, A. Nagy, & JH Waite (Geophysical Monograph 130)
- Traub, W. A., & Stier, M. T. 1976, *Applied Optics*, 15, 364
- Twarowski, A. 1995, *Combustion and flame*, 102, 41
- Venot, O. 2012, PhD Thesis, status: published
- Venot, O., Hébrard, E., Agúndez, M., et al. 2012, *A&A*, 546, A43
- Visscher, C., Lodders, K., & Fegley, Jr., B. 2006, *ApJ*, 648, 1181
- Wakeford, H. R., Sing, D. K., Deming, D., et al. 2013, *MNRAS*, 435, 3481
- Wakeford, H. R., Sing, D. K., Kataria, T., et al. 2017, in *American Astronomical Society Meeting Abstracts*, Vol. 229, *American Astronomical Society Meeting Abstracts*, 401.01
- Wang, D., Gierasch, P. J., Lunine, J. I., & Mousis, O. 2015, *Icarus*, 250, 154
- Wang, D., Lunine, J. I., & Mousis, O. 2016, *Icarus*, 276, 21
- Wilson, P. A., Sing, D. K., Nikolov, N., et al. 2015, *MNRAS*, 450, 192
- Wong, M. H., Mahaffy, P. R., Atreya, S. K., Niemann, H. B., & Owen, T. C. 2004, *Icarus*, 171, 153
- Zahnle, K., Marley, M. S., Freedman, R. S., Lodders, K., & Fortney, J. J. 2009, *ApJL*, 701, L20
- Zahnle, K., Marley, M. S., Morley, C. V., & Moses, J. I. 2016, *ApJ*, 824, 137

Table 1. Parameters for computing noise - extension of Table 4 in [Greene et al. \(2016\)](#)

Instrument	Mode	λ (μm)	native R	A_{pix} (arcsec^2) ^a	n_{pix} ^b	b ($\text{e}^- \text{s}^{-1} \text{arcsec}^{-2}$) ^c	N_d (CDS)	n_{groups}	noise floor (ppm) ^d
NIRCam	LW grism F322W2	2.5–3.9	1200@2.5 μm	0.064" \times 0.064"	4	203.62	18	12	30
NIRCam	LW grism F444W	3.9–5.0	1550@4.5 μm	0.064" \times 0.064"	4	308.74	18	25	30
MIRI	Slitless LRS prism	5.0–11.0	40@5 μm , 160@10 μm	0.110" \times 0.110"	4	5156.0	46	8	50

^a<http://www.stsci.edu/jwst/instruments/>

^btwo times the spatial extent of point source spectrum

^cThe background photon rate is computed at the JWST exposure time calculator <https://demo-jwst.etc.stsci.edu/>

^dThe adopted noise floor values are from [Greene et al. \(2016\)](#).

Table 2. Fiducial planetary system parameters in the model

T_{eq} (K)	M_p (M_J)	R_p (R_J)	a_{semi} (AU)	P (days)	T_* (K)	R_* (R_\odot)	T_{14} (s)	D (pc)	K (mag)
500	1.0	1.0	0.310	63.1	5700	1.0	26000	50	6.8
750	1.0	1.0	0.138	18.7	5700	1.0	17333	50	6.8
1000	1.0	1.0	0.0776	7.89	5700	1.0	13000	50	6.8
1500	1.0	1.0	0.0345	2.34	5700	1.0	8666	50	6.8
2000	1.0	1.0	0.0194	0.986	5700	1.0	6500	50	6.8

Table 3. Observing parameters for the planetary system in Table 2 with $T_{\text{eff}} = 500$ K.

	No. of groups per integration	No. of integrations per occultation	No. of transits	observing efficiency	transit duration
NIRCam F322W2	12	11744	2	84.6%	7.2 hrs
NIRCam F444W	25	5872	2	92.3%	7.2 hrs
MIRI LRS	8	36340	2	77.8%	7.2 hrs

Table 4. Observing parameters for the planetary system in Table 2 with $T_{\text{eff}} = 1500$ K.

	No. of groups per integration	No. of integrations per occultation	No. of transits	observing efficiency	transit duration
NIRCam F322W2	12	3916	5	84.6%	2.4 hrs
NIRCam F444W	25	1958	5	92.3%	2.4 hrs
MIRI LRS	8	12112	5	77.8%	2.4 hrs

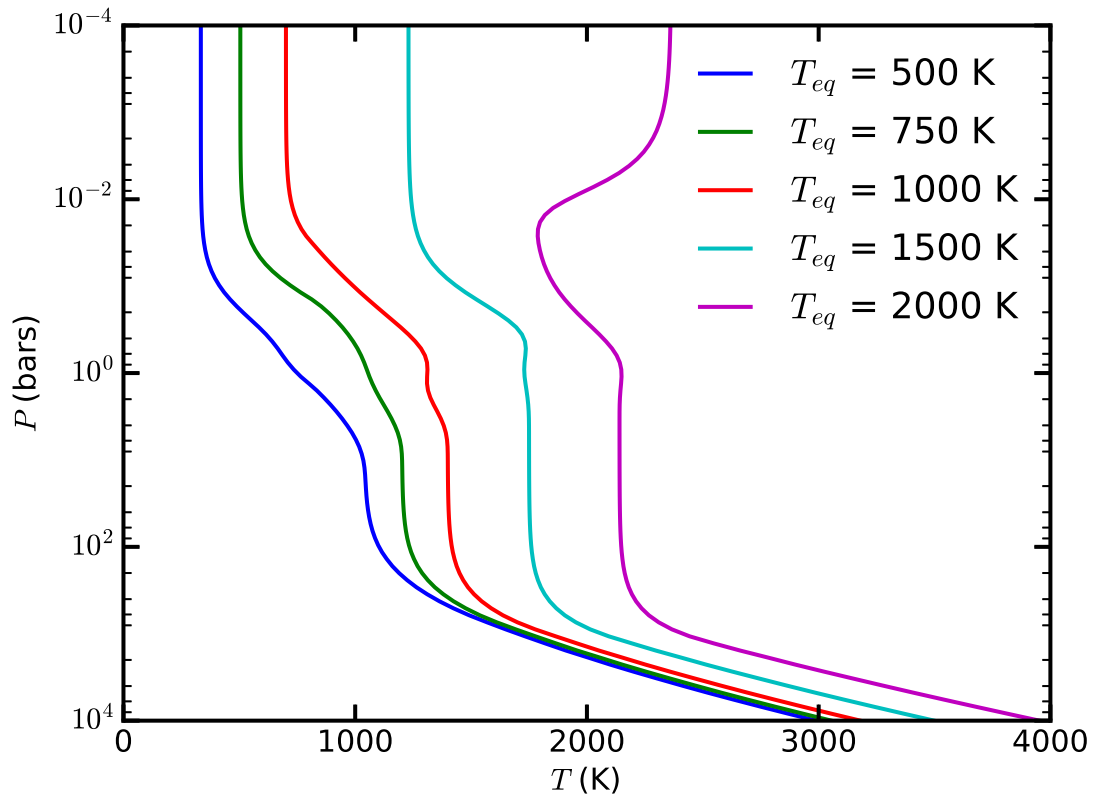


Figure 1. Horizontally-averaged temperature-pressure profile for extrasolar giant planets computed using the approach in Parmentier & Guillot (2014); Parmentier et al. (2015). Different lines correspond to different equilibrium temperatures, caused by the irradiation from the star.

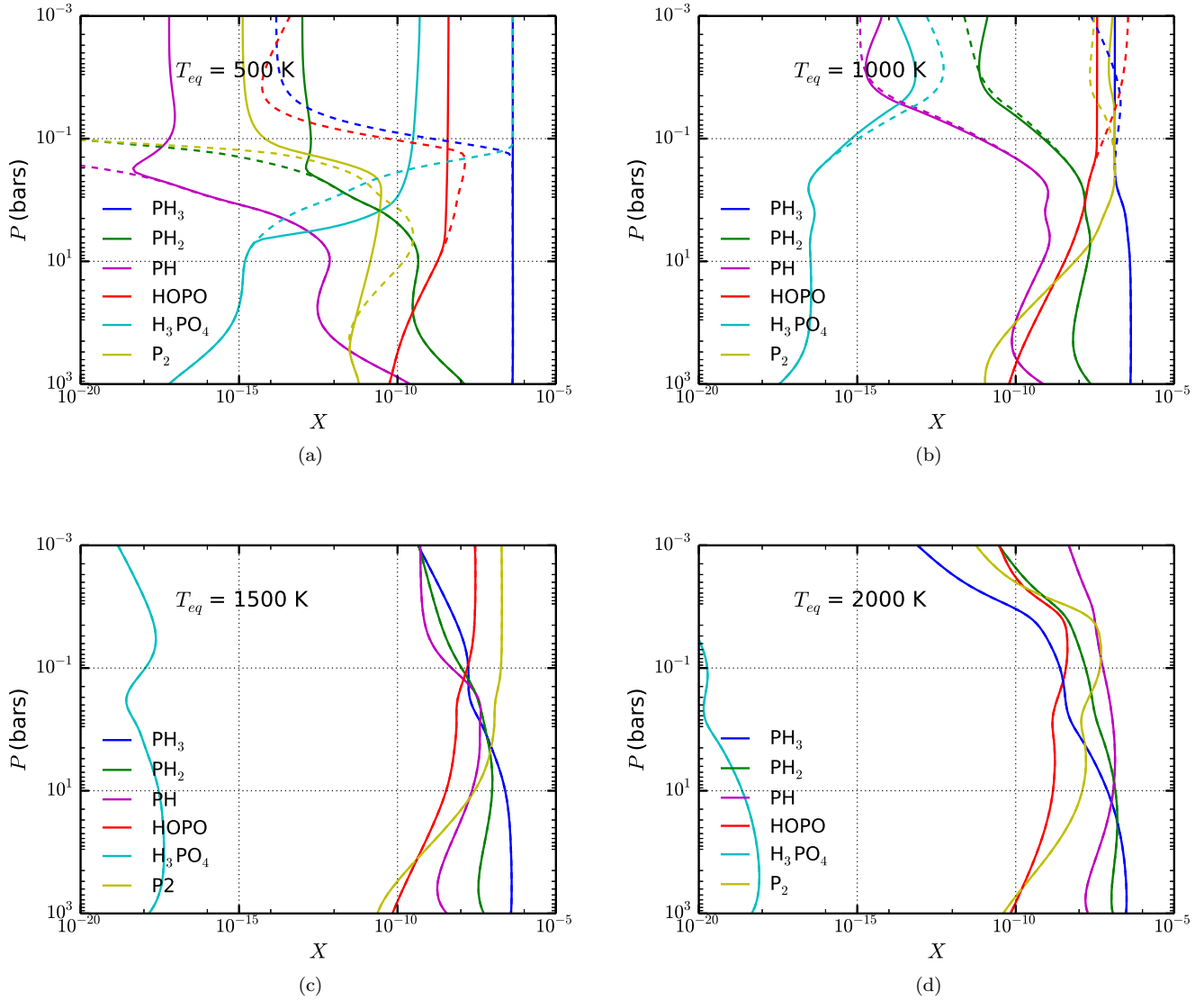


Figure 2. Computed mole fractions of major phosphorus-bearing species (PH_3 , PH_2 , PH , HOPO , H_3PO_4 , and P_2) in solar composition atmospheres. Solid lines show the abundances including the effect of vertical mixing, and the dashed lines show the abundances assuming local chemical equilibrium. The four plots correspond to different equilibrium temperatures: (a) $T_{eq} = 500$ K, (b) $T_{eq} = 1000$ K, (c) $T_{eq} = 1500$ K, (d) $T_{eq} = 2000$ K. The elemental abundance is assumed to be one solar. The eddy diffusion coefficient K_{eddy} is set at $1 \times 10^9 \text{ cm}^2\text{s}^{-1}$. Due to the lack of photodissociation modeling, the profiles are valid below ~ 0.1 bar.

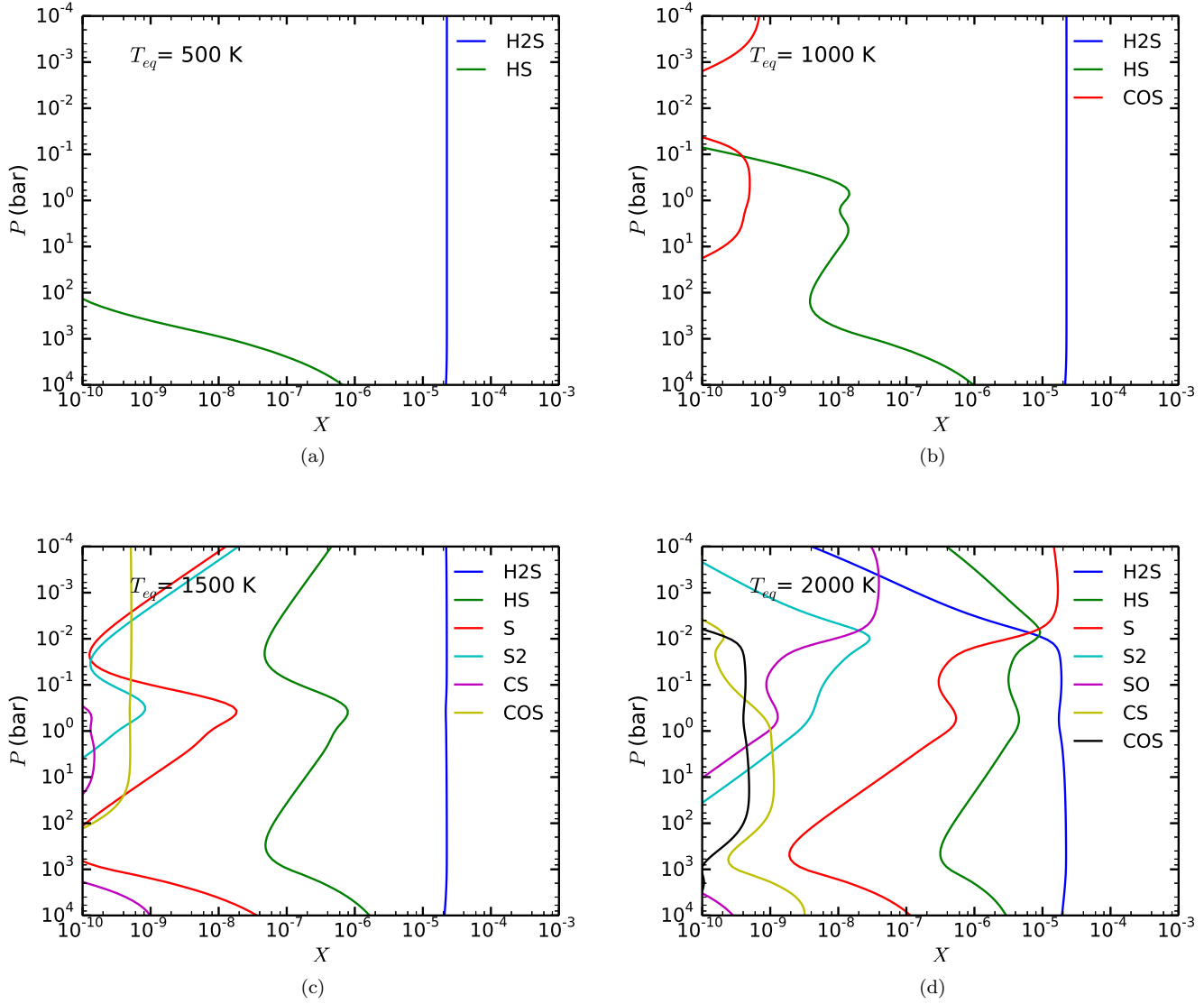


Figure 3. Computed equilibrium mole fractions of major sulfur-bearing species in solar composition atmospheres. The four plots correspond to different equilibrium temperatures: (a) $T_{eq} = 500$ K, (b) $T_{eq} = 1000$ K, (c) $T_{eq} = 1500$ K, (d) $T_{eq} = 2000$ K. The elemental abundance used here is one solar. The plot neglects the effects of photodissociation of H₂S, which may decrease the abundance of H₂S at $p < 0.01$ bar.

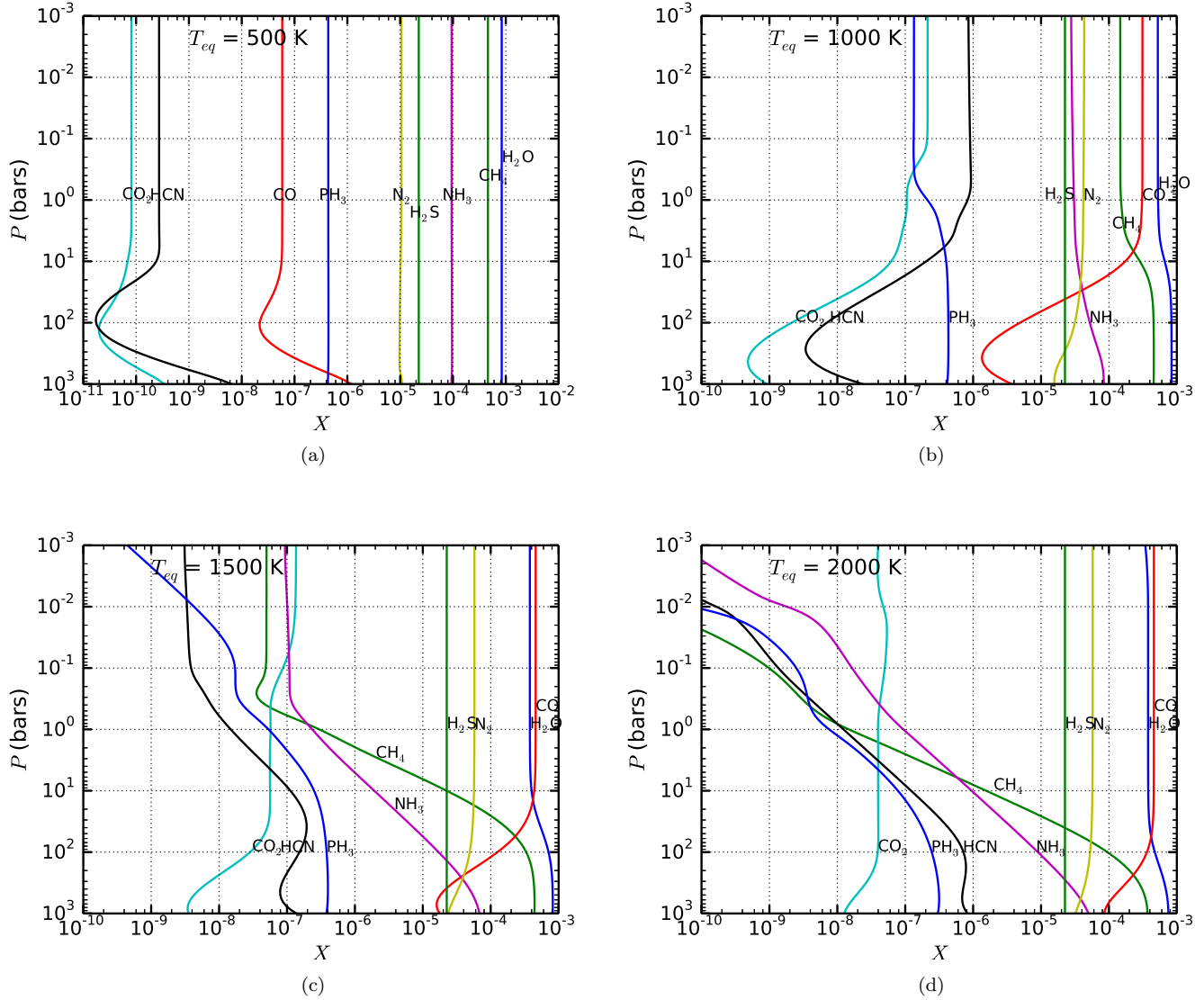


Figure 4. Computed mole fractions of major C/N/O/S/P bearing species in solar composition atmospheres including the effect of vertical mixing. The four plots correspond to different equilibrium temperatures: (a) $T_{eq} = 500$ K, (b) $T_{eq} = 1000$ K, (c) $T_{eq} = 1500$ K, (d) $T_{eq} = 2000$ K. The elemental abundance used here is one solar. The vertical eddy diffusion coefficient used here is $K_{\text{eddy}} = 1 \times 10^9 \text{ cm}^2 \text{ s}^{-1}$. The photodissociations of H_2O , CH_4 or NH_3 are expected to affect the profiles above $p \sim 0.01$ bar level, which is not included in this plot.

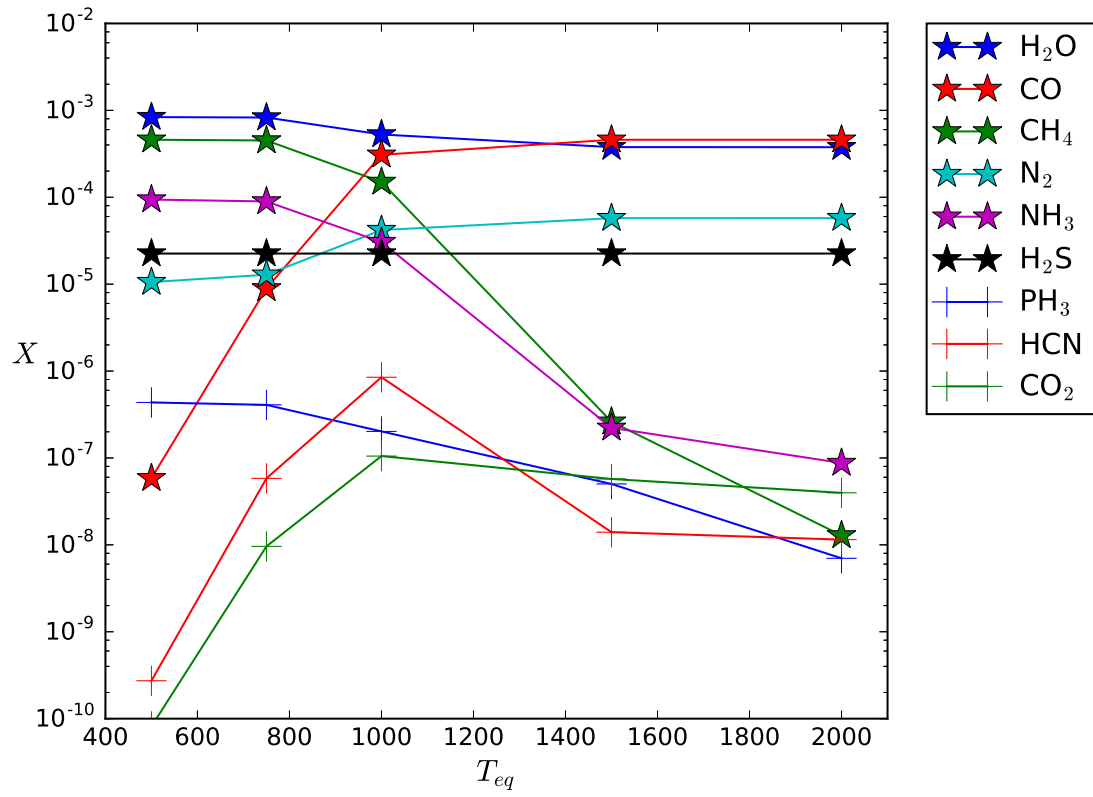


Figure 5. Mole fractions at 1 bar as a function of the equilibrium temperatures of atmospheres. The species plotted are H₂O, CO, CH₄, CO₂, NH₃, N₂, HCN, H₂S, and PH₃.

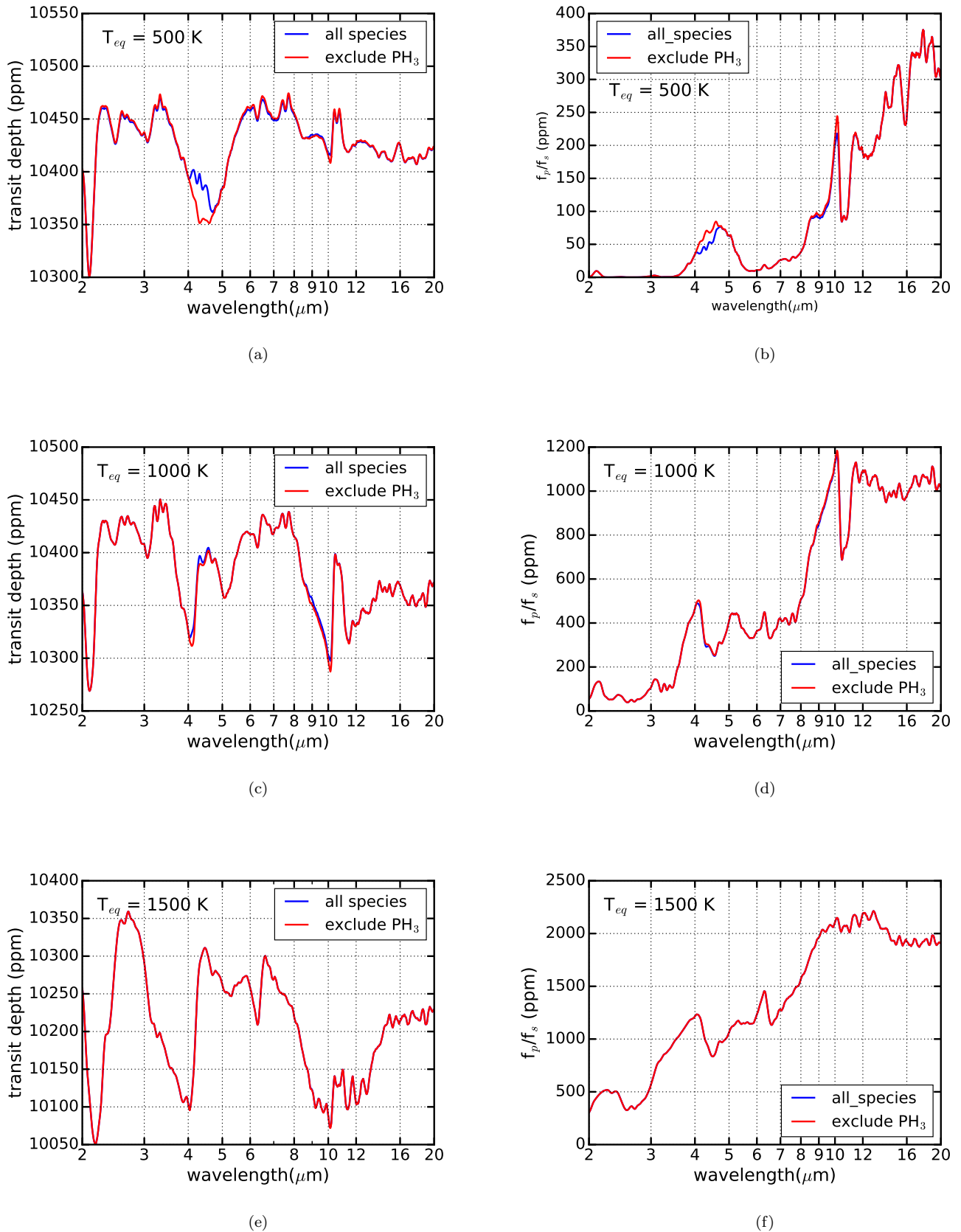


Figure 6. Simulated transmission and emission spectra for *all species* (including H_2O , CO , CH_4 , CO_2 , NH_3 , N_2 , HCN , H_2S , and PH_3) compared with *all species except PH_3* . The difference between the blue curve and the red curve indicates the absorption from PH_3 . The spectra are smoothed to a resolution of 100.

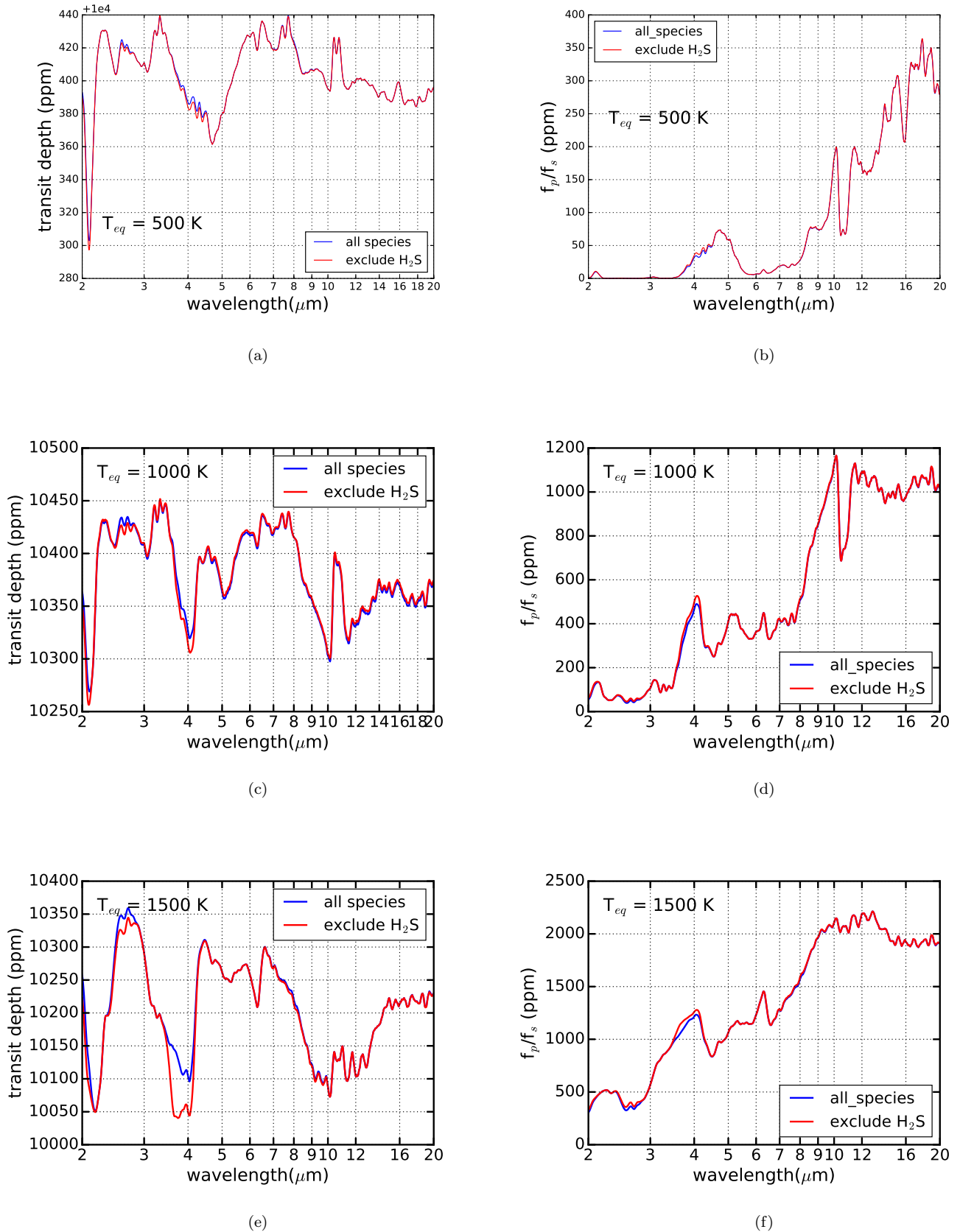


Figure 7. Simulated transmission and emission spectra for *all species* (including H₂O, CO, CH₄, CO₂, NH₃, N₂, HCN, H₂S, and PH₃) and *all species except H₂S*. The difference between the red curve and the blue curve indicates the absorption by H₂S. The spectra is smoothed to a resolution of 100.

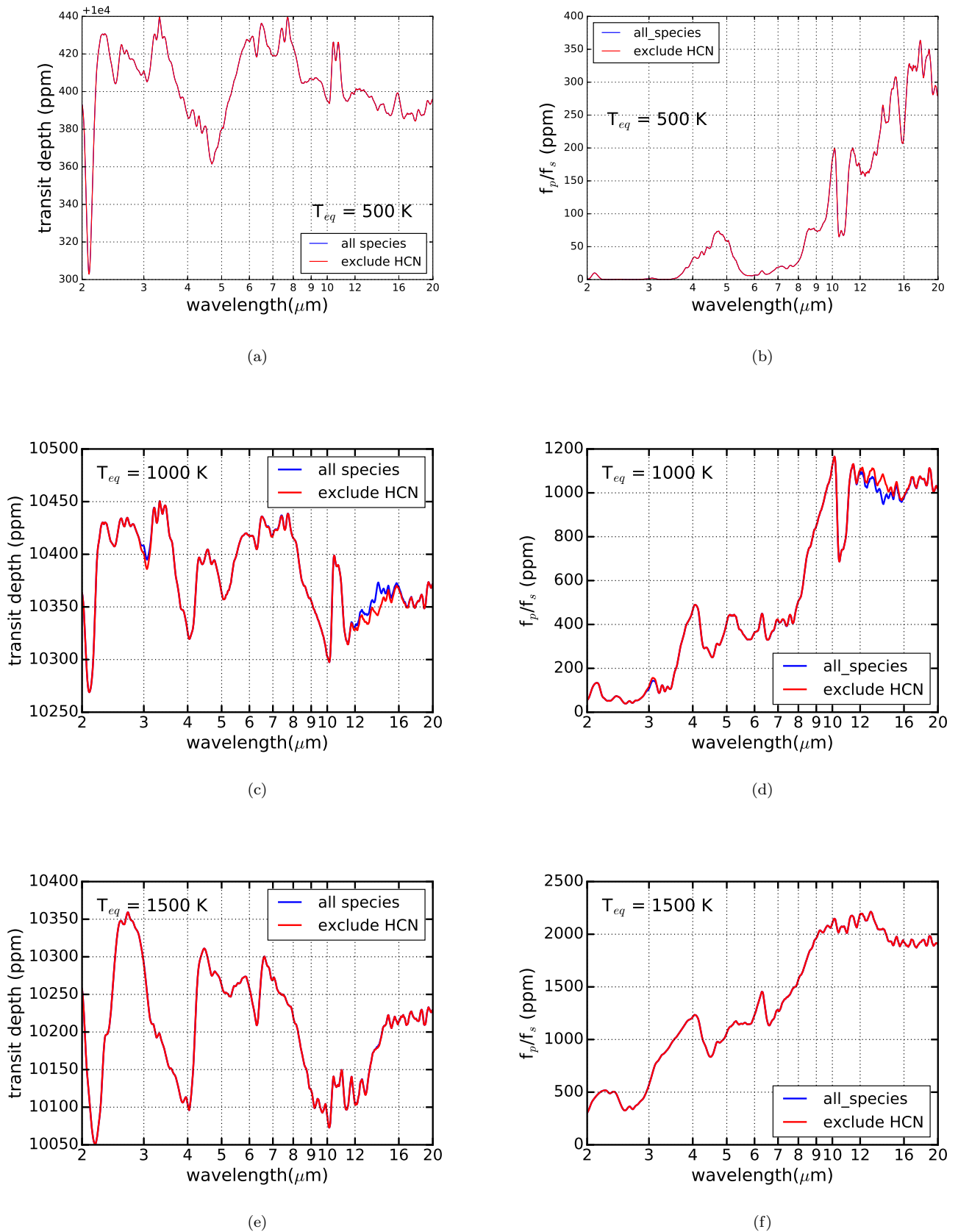


Figure 8. Simulated transmission and emission spectra for *all species* (H_2O , CO , CH_4 , CO_2 , NH_3 , N_2 , HCN , H_2S , and PH_3) and *all species except HCN*. The difference between the red curve and the blue curve indicates the absorption by HCN. The spectra is smoothed to a resolution of 100.

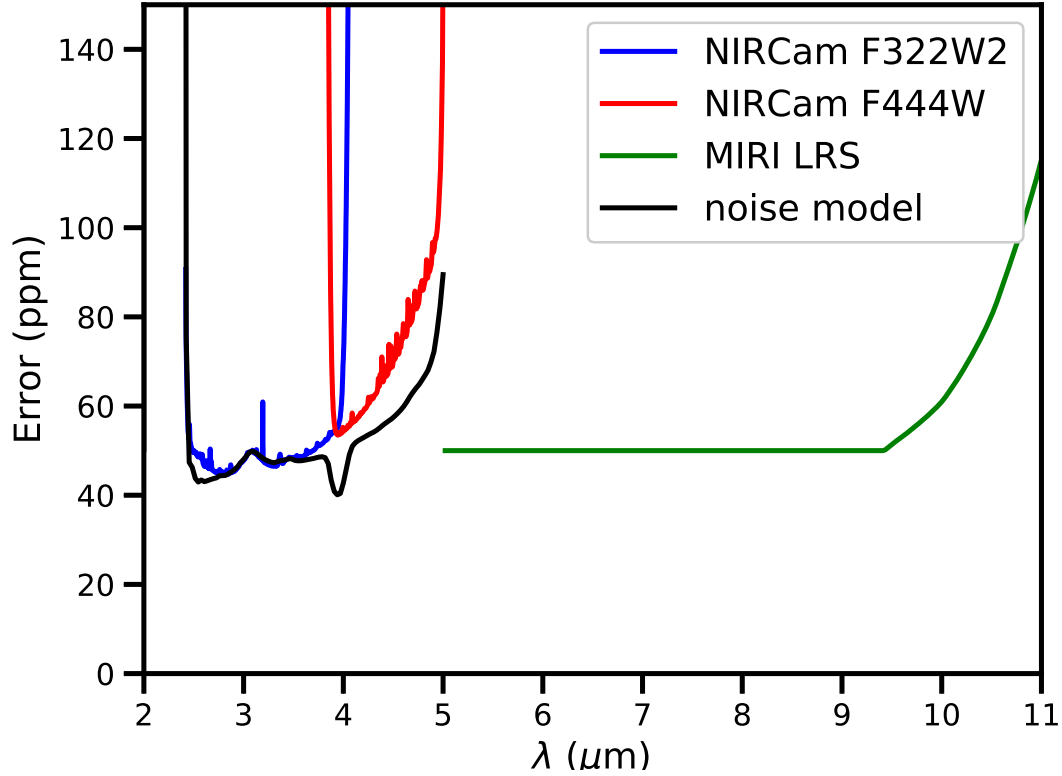


Figure 9. Noise level for different observing modes as calculated using PandExo. The target is K = 6.8 G type star. The transit duration for this calculation is 7.2 hrs. As a comparison, we also plot the error level as calculated following the recipe in Greene et al. (2016).

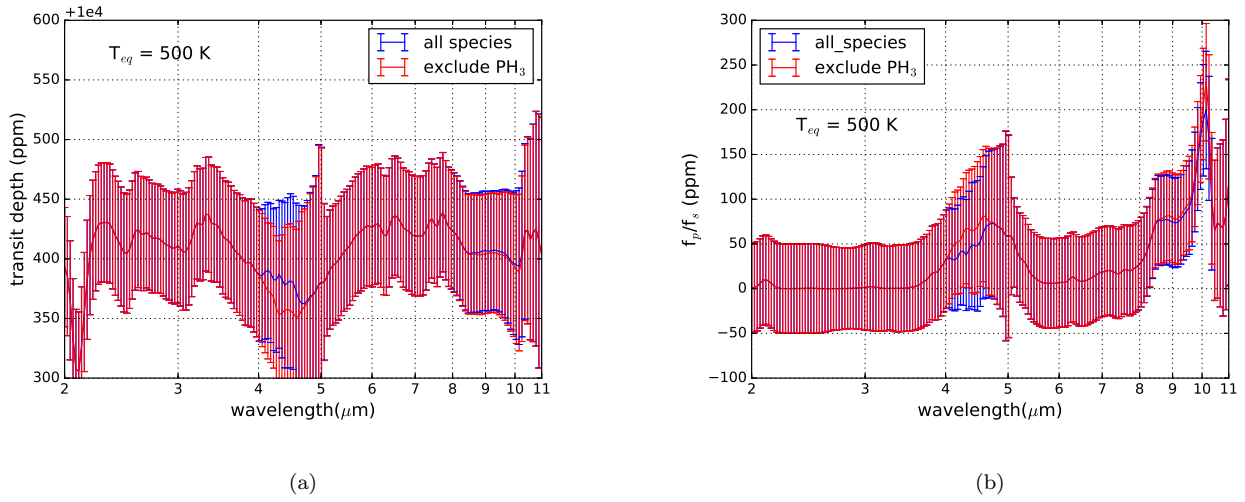


Figure 10. Synthetic transmission and emission spectra with simulated JWST noise for the planet presented in Table 2 with $T_{eq} = 500$ K. The blue curve is the binned spectra simulated including all nine species, and the red curve is the binned spectra simulated including all nine species except PH_3 . The error bars in the plot indicate one sigma Gaussian noise level simulated for JWST instrument modes summarized in Table 1. The total required observing time is 28.8 hrs.

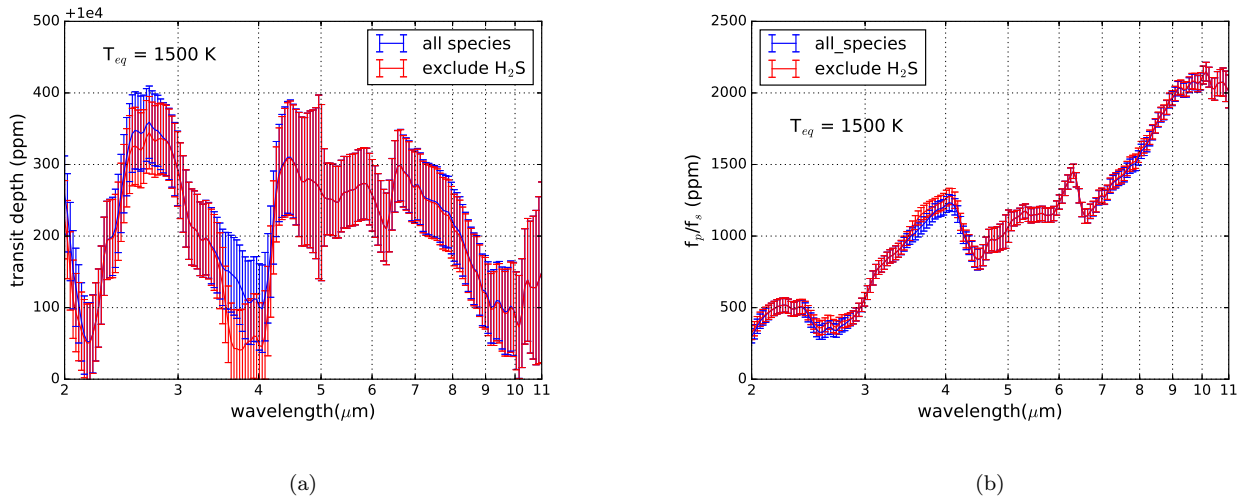


Figure 11. Synthetic transmission and emission spectra with simulated JWST noise for planet presented in Table 2 with $T_{eq} = 1500$ K. The blue curve is the binned spectra simulated including all nine species in Fig. 4, and the red curve is the binned spectra simulated including all nine species except H_2S . The error bars in the plot indicate one sigma Gaussian noise level simulated for JWST instrument modes summarized in Table 1. The total required observing time is 24.0 hrs.

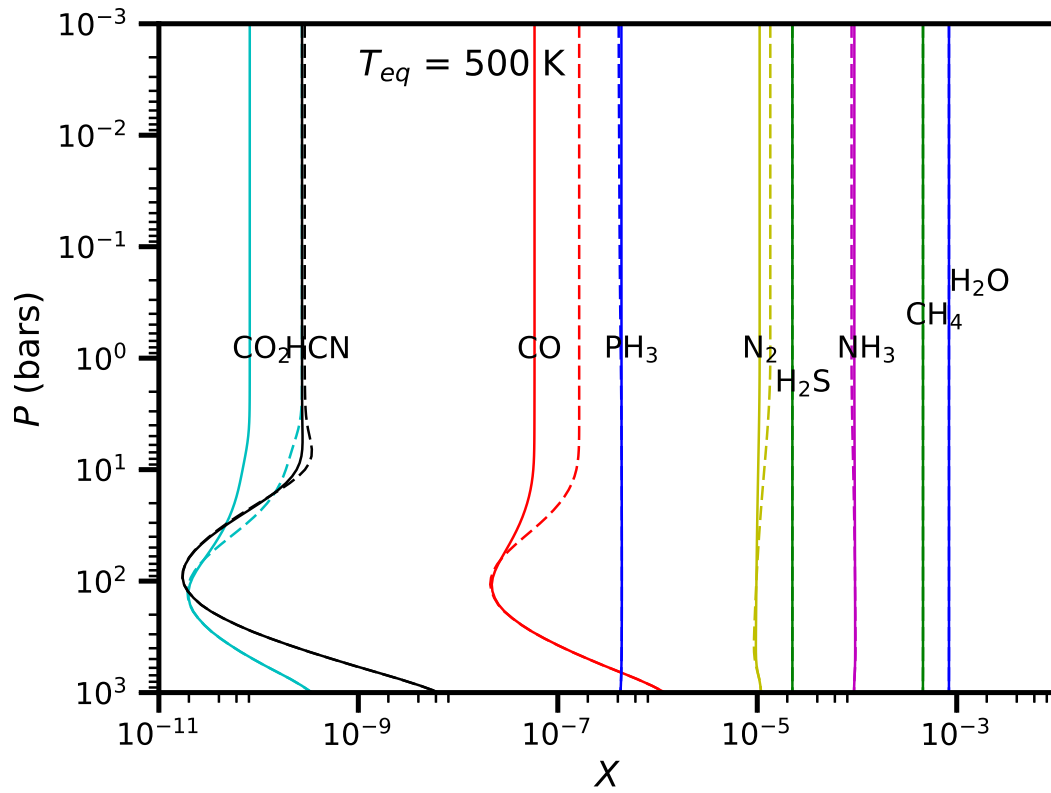


Figure 12. Comparison on the vertical profiles of major molecules between two different levels of vertical mixing. Solid lines correspond to $K_{\text{eddy}} = 1.0 \times 10^9 \text{ cm}^2 \text{ s}^{-1}$, and dashed lines correspond to $K_{\text{eddy}} = 1.0 \times 10^8 \text{ cm}^2 \text{ s}^{-1}$. The planet being modeled has solar composition atmosphere with $T_{\text{eq}} = 500 \text{ K}$.